Nanoscale

Accepted Manuscript

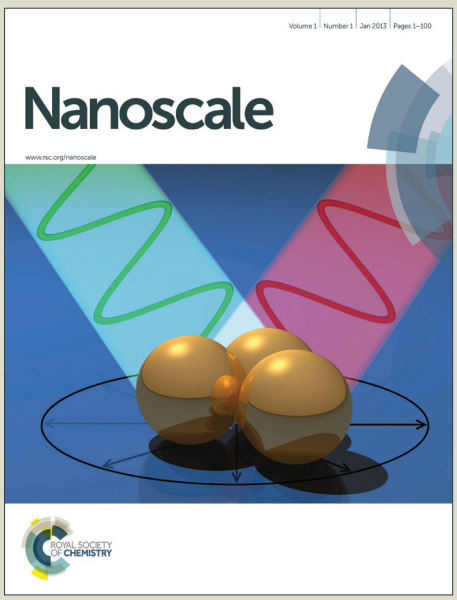

ROYAL SOCIETY OF CHEMISTRY

www.rsc.org/nanoscale

Cite this: DOI: 10.1039/c0xx00000x

www.rsc.org/xxxxxx

ARTICLE TYPE

Fog-like fluffy structured N-doped carbon with superior oxygen reduction reaction performance to commercial Pt/C catalyst

Chenghang You[a], Xiaoyuan Zen[a], Xiaochang Qiao[a], Fangfang Liu[a], Ting Shu[a], Li Du[a], Jianhuang Zeng[a], Shijun Liao[a]*

Received (in XXX, XXX) Xth XXXXXXXXX 20XX, Accepted Xth XXXXXXXXX 20XX
DOI: 10.1039/b000000x

A high-performance N-doped carbon catalyst with fog-like, fluffy structure was prepared through pyrolyzing the mixture of polyacrylonitrile, melamine and iron chloride. The catalyst exhibits excellent oxygen reduction reaction (ORR) performance, with a half-wave potential 27 mV more positive than that of commercial Pt/C catalyst (-0.120 vs. -0.147 V) and a higher diffusion-limiting current density than that of Pt/C (5.60 vs. 5.33 mA cm^{-2}) in an alkaline medium. Moreover, it also shows outstanding methanol tolerance, remarkable stability and nearly 100% selectivity for the four-electron ORR process. To our knowledge, it is one of the most active doped carbon ORR catalysts in alkaline media to date. By comparing catalysts derived from the precursors containing different amounts of melamine, we found that the added melamine not only gives the catalyst fluffy structures but also modifies the N content and the distribution of N species in the catalyst, which we believe to be the origins for the catalyst's excellent ORR performance.

Introduction

Doped carbon catalysts have attracted a great deal of attention in recent years because of their high oxygen reduction reaction (ORR) performance, low cost, and potential to replacing Pt-based catalysts in novel electrochemical energy conversion systems[1-10], such as proton exchange membrane fuel cells (PEMFCs)[11-14], direct methanol fuel cells (DMFCs), and metal-air batteries[15-17]. The past several years have seen significant researches in this area, and great progress has been achieved. However, several challenges remain before these catalysts are ready for practical applications, one key issue being that their ORR activity and stability remain insufficient. Thus, developing doped carbon catalysts with better ORR performance and stability is of great importance for the commercialization of novel electrochemical energy conversion systems.

To this end, some researchers have enhanced their catalysts' ORR performance by tuning the catalysts' composition through doping carbon with various heteroatoms, such as N, S, F, and P[5, 6, 18, 19], and by introducing transient metals, such as Fe, Co, and others[20-23]. Their work has also proven that the amount of a given dopant can significantly affect the ORR performance of the final catalyst. For example, by simply increasing the N content, various catalysts' ORR performance can usually be further enhanced[6, 24, 25].

Other researchers have improved ORR performance by giving their doped carbon catalysts well-defined porous structures[11, 26-30], which are believed to offer a greater number of exposed active sites as well as more efficient mass transfer[3, 31-34].

To obtain such well-defined structures, researchers usually use methods mediated by hard-templates[16, 29, 30, 35, 36] and activating processes[37-39]. However, these methods usually demand special pore-forming procedures, such as template removal or post-activation, which typically makes the preparation tedious and complex. Thus, direct pyrolysis of carbonaceous materials is an attractive prospect for the synthesis of porous carbons.

In view of the above issues, we developed a facile process for preparing a high-performance carbon-based ORR catalyst using polyacrylonitrile, ferric chloride, and melamine as precursors. The catalyst had a fog-like, fluffy, porous structure and exhibited excellent ORR performance, with a half-wave potential 27 mV more positive than that of a commercial Pt/C catalyst (-0.120 vs. -0.147 V) and a higher diffusion-limiting current density than that of Pt/C (5.60 vs. 5.33 mA cm^{-2}) in an alkaline medium. The catalyst also showed outstanding methanol tolerance, remarkable stability, and nearly 100% selectivity for the four-electron ORR process. To our knowledge, it is one of the most active doped carbon ORR catalysts in alkaline media to date. By comparing catalysts derived from the precursors and containing different amounts of melamine, we found that adding melamine not only gives the catalyst fluffy structures but also modifies the N content and the distribution of N species in the catalyst, which we believe to be the origins for the catalyst's excellent ORR performance.

Experimental

Preparation of materials

The catalysts were prepared through a direct pyrolysis process,

using blends of three precursors: polyacrylonitrile (PA), ferric chloride ($FeCl_3$), and melamine. A typical preparation was as follows. At 100 ºC, 2.12 g PA and 0.65 g $FeCl_3$ (with a mole ratio of PA to $FeCl_3$ being approximately 6:1) were dissolved in 100 mL dimethylformamide (DMF) to form a homogeneous solution. Next, 50 g melamine was added slowly under vigorous stirring until a thick slurry was obtained, which was then dried at 100 ºC for 24 h and grounded into powder. The obtained powder blend was then programmatically heated and pyrolyzed at 900ºC for 1 h in an Ar flow, followed by leaching with hydrochloric acid solution to remove acid-soluble components and vacuum drying at 50ºC overnight. The prepared catalyst is denoted as CPAM-50, in which "M-50" indicates the amount of melamine used in the preparation. The other samples (CPAM-30 and CPA) were prepared using similar procedures but with different amounts of melamine in the precursors.

Characterization

Scanning electron microscopy (SEM) was conducted on a MERLIN field emission scanning electron microscope (Carl Zeiss, Germany). Transmission electron microscopy (TEM) images were recorded on a JEM-2100 transmission electron microscope (JEOL, Japan). X-ray photoelectron spectroscopy (XPS) was performed on an ESCALAB 250 X-ray photoelectron spectrometer (Thermo Scientific, USA). Specific surface areas and pore-size distributions were measured by Brunauer-Emmett-Teller (BET) nitrogen adsorption-desorption at 77 K on a TriStar II 3020 gas adsorption analyzer (Micromeritics, USA). Thermogravimetric analysis (TGA) of the precursors was performed under Ar flow at a heating rate of 10ºC min^{-1} on an SDT Q600 simultaneous thermal analyzer (TA Instruments, USA).

Electrochemical testing

Electrochemical measurements were conducted in a standard three-electrode glass cell on an electrochemical workstation (Ivium, Netherlands) at room temperature, coupled with a rotating disk electrode (RDE) system (Pine Research Instrumentation, USA). A glassy carbon electrode (GCE, with a diameter of 5 mm and an electrode area of 0.1964 cm^2) was used as the working electrode substrate, with an Ag/AgCl/KCl (3 M) electrode and a Pt wire as the reference electrode and counter electrode, respectively. For simplicity, the Ag/AgCl/KCl (3 M) reference electrode is hereafter abbreviated to Ag/AgCl.

Before every measurement, the GCE surface was cleaned by ultrasonication in ethanol and polishing with α-Al_2O_3 slurry (50 nm) on a microcloth, followed by rinsing with deionized (DI) water and drying under an infrared lamp.

A slurry of the active material was prepared by mixing, under ultrasonication, 5.0 mg catalyst with 1 mL of an ethanol solution containing Nafion (0.25 wt%). Next, 20 μL catalyst slurry was pipetted onto the surface of the GCE, followed by drying under an infrared lamp to form a catalyst film on the GCE substrate. The catalyst loading was approximately 0.5 mg cm^{-2}.

Linear sweep voltammetry (LSV) measurements were conducted in a 0.1 M KOH solution at a scan rate of 5 mV s^{-1}. The LSV curves were recorded at a disk rotation rate ranging from 1600 to 3600 rpm. Before every measurement, the KOH solution was saturated with pure N_2 (99.999%) or pure O_2 (99.999%) for at least 30 min. All the current densities were normalized to the geometric area of the GCE. The chronoamperometric response was obtained at –0.3 V (vs. Ag/AgCl) in an O_2-saturated 0.1 M KOH solution. For comparison, a commercial Pt/C electrode (20 wt% Pt, Johnson Matthey, UK) was also tested under the same conditions.

The electron transfer number per oxygen molecule involved was calculated based on the Koutecky-Levich (K-L) equation, as follows:

$$J^{-1} = J_L^{-1} + J_K^{-1} = B^{-1}\omega^{-1/2} + J_K^{-1}$$

$$B = 0.62nFC_0D_0^{2/3}\nu^{-1/6}$$

$$J_K = nF\kappa C_0$$

where J is the measured current density; J_K and J_L are the kinetic and diffusion-limiting current densities, respectively; ω is the angular velocity of the disk ($\omega = 2\pi N$, where N refers to the linear rotation rate); n is the electron transfer number involved in the reduction procedure of one O_2 molecule; F is the Faraday constant (F = 96,485 C mol^{-1}); C_0 is the bulk concentration of O_2; D_0 is the diffusion coefficient of O_2 in the KOH electrolyte; ν is the kinetic viscosity of the electrode; and κ is the electron transfer rate constant. We obtained n and J_K from the K–L plots' slopes and intercepts, respectively. Using the values $C_0 = 1.2\times10^{-3}$ mol L^{-1}, $D_0 = 1.9\times10^{-5}$ cm^2 s^{-1}, and $\nu = 0.01$ cm^2 s^{-1} (in 0.1 M KOH solution), we calculated the electron transfer number (n).

For the Tafel plots, the kinetic current was calculated from the mass-transport correction of the RDE using the following equation[40]:

$$I_k = | I_L I(I_L - I)^{-1} |$$

Rotating ring disk electrode (RRDE) measurements of the samples were tested using a glassy carbon disk (Pine Research Instrumentation, USA) with a polycrystalline Pt ring biased at 0.5 V (vs. Ag/AgCl) under a rotation rate of 1600 rpm. The H_2O_2 yield and the electron transfer number (n) per oxygen molecule were calculated by using the following equations[41]:

$$\eta = 200I_r (N I_d + I_r)^{-1}$$

$$n = 4I_d(I_d + I_r N^{-1})^{-1}$$

where I_r and I_d refer to the ring and disk currents, respectively, and N is the collection efficiency (0.36), which was confirmed by reducing $K_3Fe(CN)_6$.

Results and discussion

Fig. 1 presents the SEM and TEM images of the as-prepared three materials. One can observe that CPA has an irregular, bulky morphology, while CPAM-30 and CPAM-50 have much more porous structures, indicating that melamine plays an important role in the formation of these structures.

From the STEM image and the corresponding element mapping of CPAM-50, illustrated in Fig. 1e and 1f, it can be found that the C, O and N were homogeneously dispersed, indicating the N was successfully doped into the carbon lattice uniformly.

Fig. 2a shows the N_2 gas adsorption-desorption isotherms of CPA, CPAM-30, and CPAM-50. It can be observed that the isotherms for the three catalysts all exhibit type IV curves, with hysteresis loops in the medium- and high-pressure regions, suggesting that the catalysts contain both micro- and mesoporous structures. From the pore-size distribution curves (Fig. 2b) obtained from the N_2 adsorption-desorption results, it can be

observed that CPAM-50 has the highest pore density in the meso- and macro- regions, while CPA has few pores in these regions. In addition, the greater the amount of melamine, the higher the pore densities for the larger pore sizes are, suggesting that these larger pores arise from the addition of melamine, which is stable at low temperature (<700 °C) but decomposible at higher temperature (>700 °C)[42, 43], leaving the space it had previously occupied empty and yielding porous structures in the carbon lattice. These porous structures, which contain an abundance of meso- and macro-pores, are believed to ease mass exchange during the ORR process and thereby improve the catalyst's ORR performance.

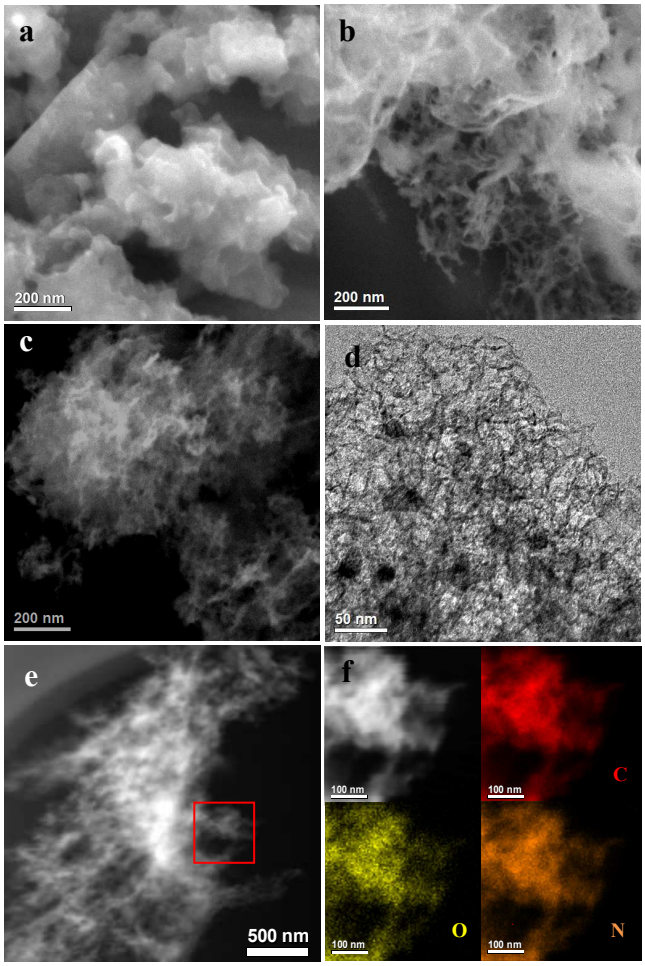

Fig. 1 SEM images: (a) CPA; (b) CPAM-30; (c) CPAM-50; (d) TEM image of CPAM-50; (e) STEM image of CPAM-50. (f) Magnified STEM image and corresponding EDS mapping of C, O and N.

With respect to surface area, CPAM-50 has the lowest BET surface area of 259 $m^2 g^{-1}$ (vs. 454 and 328 $m^2 g^{-1}$ for CPA and CPAM-30, respectively). We suggest the decrease in surface area should be attributed to the abundant macro-porous structures and the destruction of microstructures, resulting from the etching effect of the melamine decomposition products (NH_3, H_2, etc.).

Fig. 2d shows the Raman spectra of the three doped carbon catalysts. One can observe that the I_D/I_G values increase from 1.38 (CPA) to 1.42 and 1.45 for CPAM-30 and CPAM-50, indicating adding melamine in the precursors increase the number of defects among the carbon matrix, which should be also attributed to the doping and etching effects caused by melamine and its decomposed compounds.

Table 1 details the surface composition of the three catalysts obtained from the XPS results (Fig. S2). It can be observed that the N content increases with the amount of melamine used: CPAM-50 has the highest N content of 2.67 at%, while CPA has the lowest of 1.61 at% (vs. 2.29 at% for CPAM-30). This difference, we suggest, should origin from the melamine and its N-containing decomposition products that arise at high temperature.

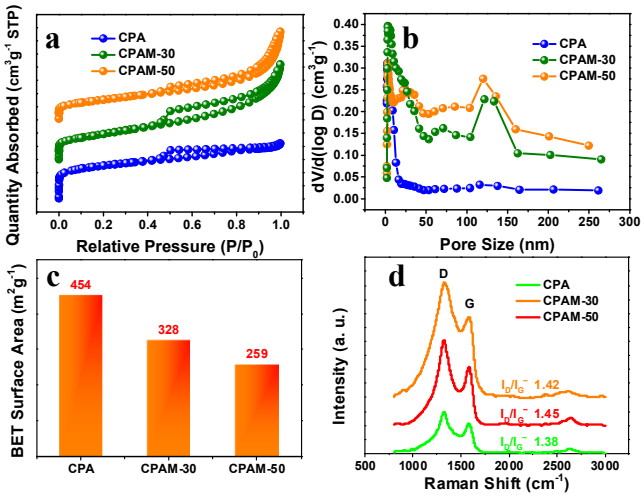

Fig. 2 (a) N_2 adsorption-desorption isotherms for CPA, CPAM-30, and CPAM-50; (b) pore-size distribution for CPA, CPAM-30 and CPAM-50; (c) BET surface areas of the three materials; (d) Raman spectra for CPA, CPAM-30 and CPAM-50.

Fig. 3a-c presents the high-resolution N1s XPS spectra and the deconvolution results for the three catalysts. Fig. 3d indicates the amount of each N species, as obtained from the deconvolution results. Clearly, the pyridinic N content was enhanced after the introduction of melamine, increasing from 19.9 at% in CPA to 30.5 at% and 37.0 at% in CPAM-30 and CPAM-50, respectively. Moreover, adding melamine also seems to have inhibited the formation of inactive oxidized N, as the relative amount of oxidized N decreased from 25.7 at% in CPA to 17.2 at% and 6.1 at% in CPAM-30 and CPAM-50, respectively.

Based on the characterization results, it can be concluded that adding melamine as a precursor can both endow the catalysts with fluffy, porous structures and affect the catalysts' compositions (especially in terms of the active N species). One can also predict that these differences in compositions and structures will certainly affect their ORR performance.

Table 1 Surface composition of CPA, CPAM-30, and CPAM-50

Catalyst	Species Concentration (at%)		
	C	N	O
CPA	93.17	1.61	4.29
CPAM-30	91.35	2.29	6.36
CPAM-50	92.21	2.67	5.12

Fig. 4a illustrates the LSV curves of the three catalysts in O_2-saturated 0.1 M KOH solution at an electrode rotation rate of 1600 rpm. Clearly, after melamine was introduced, the ORR catalytic performance was drastically enhanced, with half-

potentials shifted positively by 34 and 57 mV to -0.14 and -0.12 V for CPAM-30 and CPAM-50, respectively. We attribute these results to the fluffy, porous structures and modified distribution of active N species induced by melamine. In comparison to the commercial Pt/C catalyst's ORR performance, that of CPAM-50 was obviously superior, with a half-wave potential 27 mV more positive (-0.120 vs. -0.147 V) and a higher diffusion-limiting current density (5.60 vs. 5.33 mA cm^{-2}). To our knowledge, CPAM-50 is also one of the best doped carbon catalysts for the ORR in alkaline medium to date.

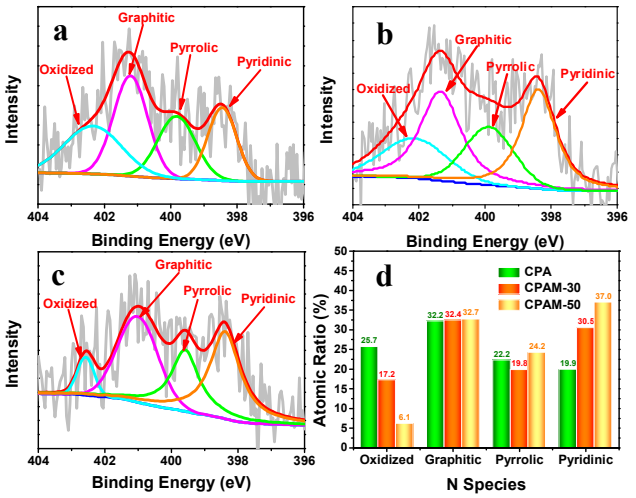

Fig. 3 (a) N1s XPS spectrum for CPA. (b) N1s XPS spectrum for CPAM-30. (c) N1s XPS spectrum for CPAM-50. (d) Atomic ratio of each N species in the three catalysts.

Fig. 4b shows the three catalysts' Tafel plots: 61, 68, and 104 mV dec^{-1}. The lowest Tafel slope of CPAM-50 confirms its superior ORR performance and further suggests that CPAM-50 has the lowest overpotential among the three catalysts.

To further understand the kinetics of the ORR involving our catalysts, their LSV curves in O_2-saturated solution under various rotation rates (See Fig 3S) were recorded and further analyzed using the K-L equation, permitting us to calculate the exact electron transfer numbers of the three catalysts, which are summarized in Fig. 5d. Evidently, the two catalysts derived from melamine-containing precursors have higher electron transfer numbers than CPA. The electron transfer number of approximately four for CPAM-30 and CPAM-50 suggests that oxygen can be directly reduced to OH^- without producing intermediate OOH^-. The lower electron transfer number (around 3.5) for CPA means that it can only catalyze the ORR through a path that combines two-electron and four-electron processes. That is, CPAM-30 and CPAM-50 have much higher catalytic efficiency than CPA, indicating that adding melamine can drastically improve CPA's efficiency.

To confirm the ORR pathways of the three catalysts, RRDE measurements were then conducted. As illustrated in Fig. 4d and 4e, CPAM-50 has the highest "*n*" values of above 3.9 and the lowest hydro peroxide yield between 2% to 6% over the potential range of -0.2 to -0.8 V (vs. Ag/AgCl), while CPA has the lowest "*n*" values and the highest hydro peroxide yields at the same potential window, consistent with the results obtained by K-L analysis.

Regarding the relationship between current density and rotation rate (Fig. 4f), it is interesting to find that all three catalysts' current densities are almost proportional to the rotation rates, and CPAM-50 has the lowest slope (0.205), while CPA has the highest (0.257). That is, CPAM-50 is the most insensitive to the changes of rotation rates. These results might also imply that the mass transfer in CPAM-50 is better than in CPA and CPAM-30, which would be the certain result of their various porous structures, as affected by the addition of melamine.

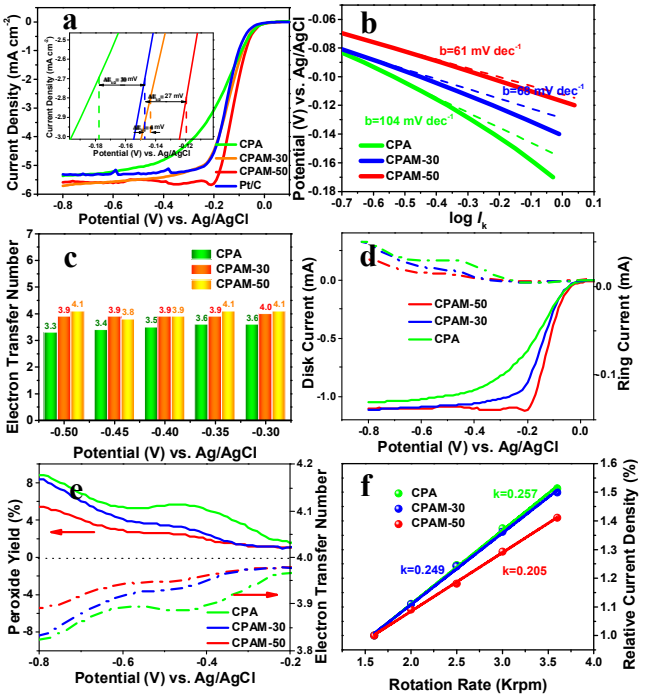

Fig. 4 (a) LSV curves of CPA, CPAM-30, and CPAM-50. (b) Tafel plots of the prepared catalysts. (c) Electron transfer numbers at different potentials. (d) RRDE disk and ring current with rotation rate of 1600 rpm in 0.1 M KOH. (e) Peroxide yields and electron transfer number of the catalysts vs. potential calculated from the RRDE measurement results. (f) The relationship between relative current density at –0.5 V (vs. Ag/AgCl) and rotation rates. The relative current density results were obtained by normalizing the current density values at different rotation rates with the ones under1600 rpm.

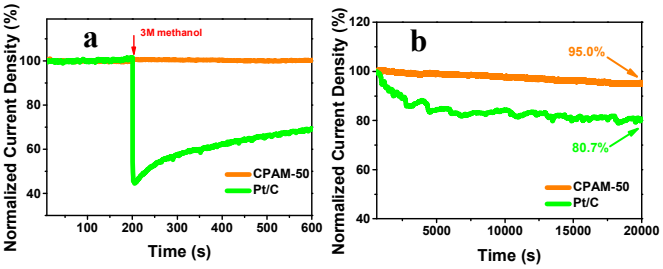

Fig. 5 (a) Current–time (i–t) chronoamperometric responses of CPAM-50 and commercial 20% Pt/C electrodes upon the introduction of 3 M methanol. (b) current–time (i–t) chronoamperometric responses of CPAM-50 and commercial 20% Pt/C electrodes at –0.3 V in O_2-saturated 0.1 M KOH at a rotation rate of 1600 rpm.

Fig. 5 indicates that as well as high ORR performance, our catalyst also exhibits excellent methanol tolerance and

outstanding stability. As shown in Fig. 5a, the ORR performance of commercial Pt/C catalyst dropped noticeably when methanol was introduced, whereas almost no change was observed for CPAM-50, suggesting that the latter has much higher methanol tolerance.

Fig. 5b illustrates CPAM-50's excellent stability. After 20,000 s of continuous ORR at –0.3 V (vs. Ag/AgCl), CPAM-50 maintained more than 95% of its initial ORR performance, whereas Pt/C lost almost 20% of its initial current density under the same conditions.

Conclusion

In this work, we successfully fabricated a high-performance N-doped carbon catalyst with a hierarchically porous structure through a direct pyrolysis process using polyacrylonitrile, melamine, and iron chloride as precursors. The catalyst exhibits a fog-like, fluffy, porous structures and excellent ORR performance, with a half-wave potential 27 mV more positive than that of Pt/C catalyst (-0.120 vs. -0.147 V) and a higher diffusion-limiting current density than that of Pt/C (5.60 vs. 5.33 mA cm^{-2}) in an alkaline medium. In addition, the catalyst shows outstanding methanol tolerance, remarkable stability, and nearly 100% selectivity for the four-electron ORR process. To our knowledge, it is also one of the most active ORR catalysts in alkaline media to date. By comparing catalysts fabricated with different amounts of melamine precursors, we determined that melamine not only induces the fluffy structure but also modifies the N content and the distribution of N species in the catalysts, and we believe these factors should be responsible for the catalysts' excellent ORR performance.

The high performance, outstanding stability, and excellent methanol tolerance, combined with their highly porous morphology, will make these catalysts promising for the applications in novel, environmentally friendly electrochemical energy systems, such as PEMFCs, DMFCs, and metal-air batteries.

Acknowledgements

This work was supported by the National Science Foundation of China (NSFC Project Nos. 21076089, 21276098, 11132004, and U1301245), the Ministry of Science and Technology of China (Project No. 2012AA053402), the Guangdong Natural Science Foundation (Project No. S2012020011061), the Doctoral Fund of the Ministry of Education of China (20110172110012), and the Basic Scientific Foundation of the Central Universities of China (No. 2013ZP0013).

Notes and references

[a]*The Key Laboratory of Fuel Cell Technology of Guangdong Province, School of Chemistry and Chemical Engineering, South China University of Technology, Guangzhou, 510641, China, Fax: +86 20 8711 3586. E-mail address: chsjliao@scut.edu.cn*

†Electronic Supplementary Information (ESI) available: more experimental details, additional SEM and TEM images, linear voltammetric curves, Koutecky–Levich plots, N_2 adsorption-desorption isotherms, and pore-size distributions. See DOI: ‡

1. G. Wu, K. L. More, C. M. Johnston and P. Zelenay, *Science*, 2011, **332**, 443-447.
2. K. P. Gong, F. Du, Z. H. Xia, M. Durstock and L. M. Dai, *Science*, 2009, **323**, 760-764.
3. R. Bashyam and P. Zelenay, *Nature*, 2006, **443**, 63-66.
4. D. Deng, L. Yu, X. Chen, G. Wang, L. Jin, X. Pan, J. Deng, G. Sun and X. Bao, *Angew Chem Int Edit*, 2013, **52**, 371-375.
5. J. Y. Cheon, T. Kim, Y. Choi, H. Y. Jeong, M. G. Kim, Y. J. Sa, J. Kim, Z. Lee, T. H. Yang, K. Kwon, O. Terasaki, G. G. Park, R. R. Adzic and S. H. Joo, *Sci Rep-Uk*, 2013, **3**, 2715.
6. H. Peng, S. Hou, D. Dang, B. Zhang, F. Liu, R. Zheng, F. Luo, H. Song, P. Huang and S. Liao, *Appl Catal B - Environ*, 2014, **158**, 60-69.
7. H. L. Peng, Z. Y. Mo, S. J. Liao, H. G. Liang, L. J. Yang, F. Luo, H. Y. Song, Y. L. Zhong and B. Q. Zhang, *Sci Rep-Uk*, 2013, **3**, 1765.
8. H. T. Chung, J. H. Won and P. Zelenay, *Nat Commun*, 2013, **4**, 1922-1926.
9. D. Grumelli, B. Wurster, S. Stepanow and K. Kern, *Nat Commun*, 2013, **4**, 2904.
10. X. Yang, W. Zou, Y. Su, Y. Zhu, H. Jiang, J. Shen and C. Li, *J. Power Sources*, 2014, **266**, 36-42.
11. C. You, S. Liao, X. Qiao, X. Zeng, F. Liu, R. Zheng, H. Song, J. Zeng and Y. Li, *J Mater Chem A*, 2014, **2**, 12240 - 12246.
12. C. You, S. Liao, H. Li, S. Hou, H. Peng, X. Zeng, F. Liu, R. Zheng, Z. Fu and Y. Li, *Carbon*, 2014, **69**, 294-301.
13. X. Qiao, C. You, T. Shu, Z. Fu, R. Zheng, X. Zeng, X. Li and S. Liao, *Electrochem Commun*, 2014, **47**, 49-53.
14. F. Liu, H. Peng, C. You, Z. Fu, P. Huang, H. Song and S. Liao, *Electrochim Acta*, 2014, **138**, 353-359.
15. Z. Zhang, J. Bao, C. He, Y. Chen, J. Wei and Z. Zhou, *Adv Funct Mater*, 2014, n/a-n/a.
16. J. Li, H. M. Zhang, Y. N. Zhang, M. R. Wang, F. X. Zhang and H. J. Nie, *Nanoscale*, 2013, **5**, 4647-4651.
17. X. Huang, H. Yu, H. Tan, J. Zhu, W. Zhang, C. Wang, J. Zhang, Y. Wang, Y. Lv, Z. Zeng, D. Liu, J. Ding, Q. Zhang, M. Srinivasan, P. M. Ajayan, H. H. Hng and Q. Yan, *Adv Funct Mater*, 2014, **24**, 6516-6523.
18. Y. Zhu, B. Zhang, X. Liu, D. Wang and D. S. Su, *Angew Chem Int Edit*, 2014, **53**, 10673-10677.
19. H. Peng, F. Liu, X. Liu, S. Liao, C. You, X. Tian, H. Nan, F. Luo, H. Song, Z. Fu and P. Huang, *Acs Catal*, 2014, **4**, 3797-3805.
20. G. Q. Zhang, B. Y. Xia, X. Wang and X. W. Lou, *Adv Mater*, 2014, **26**, 2408-2412.
21. Z. Xiang, Y. Xue, D. Cao, L. Huang, J. Chen and L. Dai, *Angew Chem Int Edit*, 2014, **53**, 2433-2437.
22. Z. Xiang, D. Cao, L. Huang, J. Shui, M. Wang and L. Dai, *Adv Mater*, 2014, **26**, 3356-3356.
23. Z.-Y. Wu, P. Chen, Q.-S. Wu, L. Yang, Z. Pan and Q. Wang, *Nano Energy*, 2014, **8**, 118-125.
24. X. Zhong, L. Liu, X. Wang, H. Yu, G. Zhuang, D. Mei, X. Li and J. Wang, *J Mater Chem A*, 2014, **2**, 6703-6707.
25. S. Song, Y. Xue, L. Feng, H. Elbatal, P. Wang, C. N. Moorefield, G. R. Newkome and L. Dai, *Angew Chem Int Edit*, 2014, **53**, 1415-1419.
26. J. Liang, R. F. Zhou, X. M. Chen, Y. H. Tang and S. Z. Qiao, *Adv Mater*, 2014, **26**, 6074-6079.
27. J. Liang, Y. Zheng, J. Chen, J. Liu, D. Hulicova-Jurcakova, M. Jaroniec and S. Z. Qiao, *Angew Chem Int Edit*, 2012, **51**, 3892-3896.
28. Y. Zheng, Y. Jiao, J. Chen, J. Liu, J. Liang, A. Du, W. M. Zhang, Z. H. Zhu, S. C. Smith, M. Jaroniec, G. Q. Lu and S. Z. Qiao, *J Am Chem Soc*, 2011, **133**, 20116-20119.
29. W. Ding, Z. Wei, S. Chen, X. Qi, T. Yang, J. Hu, D. Wang, L. Wan, S. F. Alvi and L. Li, *Angew Chem Int Edit*, 2013, **125**, 11971-11975.
30. W. Wei, H. W. Liang, K. Parvez, X. D. Zhuang, X. L. Feng and K. Mullen, *Angew Chem Int Edit*, 2014, **53**, 1570-1574.
31. P. Zhang, F. Sun, Z. Xiang, Z. Shen, J. Yun and D. Cao, *Energ Environ Sci*, 2014, **7**, 442-450.
32. W. Kiciński, M. Szala and M. Bystrzejewski, *Carbon*, 2014, **68**, 1-32.
33. Y. G. Li, W. Zhou, H. L. Wang, L. M. Xie, Y. Y. Liang, F. Wei, J. C. Idrobo, S. J. Pennycook and H. J. Dai, *Nat Nanotechnol*, 2012, **7**, 394-400.
34. Z. Liu, H. G. Nie, Z. Yang, J. Zhang, Z. P. Jin, Y. Q. Lu, Z. B. Xiao and S. M. Huang, *Nanoscale*, 2013, **5**, 3283-3288.

35. J. Xu, F. He, S. Gai, S. Zhang, L. Li and P. Yang, *Nanoscale*, 2014, **6**, 10887-10895.
36. S. Yang, X. Feng, L. Wang, K. Tang, J. Maier and K. Müllen, *Angew Chem Int Edit*, 2010, **49**, 4795-4799.
37. L. Chen, Y. Zhang, C. Lin, W. Yang, Y. Meng, Y. Guo, M. Li and D. Xiao, *J Mater Chem A*, 2014, **2**, 9684-9690.
38. Q. C. Zeng, D. C. Wu, C. Zou, F. Xu, R. W. Fu, Z. H. Li, Y. R. Lianga and D. S. Su, *Chem Commun*, 2010, **46**, 5927-5929.
39. C. Zou, D. C. Wu, M. Z. Li, Q. C. Zeng, F. Xu, Z. Y. Huang and R. W. Fu, *J Mater Chem*, 2010, **20**, 731-735.
40. J. B. Xu, P. Gao and T. S. Zhao, *Energ Environ Sci*, 2012, **5**, 5333-5339.
41. J. Wang, G. Wang, S. Miao, X. Jiang, J. Li and X. Bao, *Carbon*, 2014, **75**, 381-389.
42. M. Zhong, E. K. Kim, J. P. McGann, S. E. Chun, J. F. Whitacre, M. Jaroniec, K. Matyjaszewski and T. Kowalewski, *J Am Chem Soc*, 2012, **134**, 14846-14857.
43. Y. Chang, F. Hong, C. He, Q. Zhang and J. Liu, *Adv Mater*, 2013, **25**, 4794-4799.